June 10, 2022

Digitised charged-particle discrimination in CsI detector signals

Linus Persson

Division of Nuclear Physics, Department of Physics, Lund University

Supervised by Prof. Dirk Rudolph and Yuliia Hrabar

Thesis submitted in partial fulfilment of the requirements for the degree of
Bachelor of Science in Physics

FYSK02, 15 hp (2 months full-time equivalent)

LUND
UNIVERSITY

Abstract

This work is aimed at improving the discrimination of protons and α particles in digitised signals from CsI(Tl) scintillators. This has been achieved using pulse-shape discrimination, wherein the shape of the pulses is used to learn which particle is detected. Two primary methods have been implemented and compared, namely, the charge-comparison method where the ratio between the integrals of two different regions of the pulse is calculated, and the cosine similarity measure which indicates the similarity to a reference pulse. The work has demonstrated improvements of up to 20 % in certain detector elements over the pre-existing method which utilised a simple version of the charge-comparison method. In the future, it may be beneficial to explore machine learning algorithms to further improve and automate the discrimination process.

Populärvetenskaplig beskrivning

För att förstå atomkärnans struktur är det framgångsrikt att studera exotiska kärnor med ett skevt förhållande mellan antalet protoner och neutroner. Sådana kärnor är dock mycket instabila och således svåra att bilda och analysera. Ett sätt att skapa dem är genom fusion-evaporationsreaktioner, då två kärnor kollideras och därvid sammansmälter. Den nybildade kärnan sönderfaller ögonblickligen genom emission av protoner, neutroner, alfapartiklar och gammastrålning. Av särskilt intresse är gammastrålningen, eftersom fotonernas energi återspeglar energinivåerna i den exotiska kärnan. För att kunna lista ut vilken kärna som faktiskt bildas vid en reaktion behöver emellertid de andra sönderfallsprodukterna först identifieras. Detta kräver en komplex experimentell uppställning där flera olika detektorer samverkar.

För att specifikt detektera laddade partiklar såsom protoner och alfapartiklar kan scintillationsdetektorer utnyttjas. En scintillator är ett material som avger ljus när den träffas av en inkommande partikel. Detta ljus kan omvandlas till elektriska signaler som amplifieras och lagras digitalt. Signalerna från protoner och alfapartiklar är något annorlunda, vilket gör det möjligt att urskilja de båda partikeltyperna med en teknik som kallas pulsformsdiskriminering. Syftet med arbetet som presenteras här är att förbättra separationen genom att optimera hur pulsformen analyseras.

Metoden som var implementerad före detta arbete innefattar att integrera två olika delar av pulsen. Kvoten mellan dessa båda areor är då en indikator för partikeltypen. Gränserna för integrationen har tidigare satts ganska godtyckligt och varit desamma för alla detektorer. Inom ramen för detta arbete kan olika integrationsgränser användas för olika detektorer. Vidare har en alternativ metod implementerats och analyserats, varvid pulserna som uppmäts jämförs med en referenspuls genom ett likhetsmått kallat cosinuslikhet. Därtill har en metodik för att utvärdera prestandan hos de olika metoderna formulerats och tillämpats.

Datan som detta arbete utgår ifrån har samlats in vid ett experiment på Argonne National Laboratory under sommaren 2020. Vid experimentet användes Microball, en detektoruppsättning av tallium-aktiverade CsI-scintillationsdetektorer och det är pulserna därifrån som analyserats. Genom att effektivisera urskiljningen av protoner och alfapartiklar är det möjligt att producera förbättrade gammaspektra tillhörande de atomkärnor som bildades vid reaktionen. I förlängningen kan detta förhoppningsvis bidra till nya slutsatser om atomkärnans struktur.

Acknowledgements

First and foremost, I wish to extend my thanks to my supervisor, Professor Dirk Rudolph, for introducing me to the exciting field of nuclear physics and arranging for this project to take place. Throughout the project, I have been most grateful for his willingness to engage in discussions ranging from technical matters to broader high-level planning. I also thank him for his feedback on drafts of this report.

Secondly, I wish to thank the co-supervisor, Yuliia Hrabar, for her support over the course of the semester. Particularly, I appreciate her patience in explaining how the data acquisition and sorting are performed. I have greatly enjoyed our discussions and have benefited from her general guidance. I also express my gratitude to the wider Nuclear Structure Group and the Division of Nuclear Physics for making me feel welcome in the corridor. Finally, I thank my family for their encouragement and support during my BSc studies.

Contents

List of acronyms

ANL	Argonne National Laboratory
CsI(Tl)	Thallium-activated cesium iodide
DAQ	Data acquisition system
DFMA	Digital fragment mass analyser
DSSD	Double-sided silicon strip detector
FMA	Fragment mass analyser
FOM	Figure of merit
FWHM	Full width at half maximum
IC	Ionisation chamber
PID	Particle identification
PMT	Photomultiplier tube
PPAC	Parallel-plate avalanche counter
PSD	Pulse-shape discrimination

List of figures

List of tables

1 Introduction

Atomic nuclei are characterised by their proton number (Z) and neutron number (N). By plotting these quantities against each other for all known nuclei, one receives the so-called nuclear landscape, shown in Figure 1. Only a small fraction of all possible nuclei are stable. The fundamental reason for this is the principle of minimisation of total relativistic energy. If a nucleus can somehow decay into a state of lower mass M (and corresponding relativistic rest energy Mc^2), the decay will generally happen with some probability [2, 3]. The stability of light elements is governed mainly by β decay. Free neutrons are unstable and will undergo β^- decay with a half-life of about 10 minutes according to

$$n \rightarrow p + e^- + \bar{\nu}_e + \text{energy}.$$

The released energy (0.78 MeV) is manifested in the form of kinetic energy of the decay products. If instead energy is added, the reverse reaction is possible, namely the β^+ decay

$$p + \text{energy} \rightarrow n + e^+ + \nu_e.$$

With this information at hand, one realises that nuclei with constant mass number ($A = N + Z$) may decay into one another. The differences in binding energy between nuclei can provide the energy necessary for this process to take place. For this reason, only a limited number of (N, Z) combinations are stable. Such nuclei are appropriately said to be along the line of β stability [2, 3]. One may form nuclei with an excess of protons or neutrons although they will decay with a lifetime determined by the inherent stability of the configuration, which is also affected by the detailed shell structure of the nucleonic energy levels. The ultimate outer bounds of the nuclear landscape are given by the proton and neutron drip lines. The drip lines arise once the last added proton or neutron becomes unbound, i.e., the binding energy of the nucleus decreases rather than increases with the addition of the last nucleon [2].

To gain a deeper understanding of the nuclear interaction, it is lucrative to venture beyond the line of β stability towards the drip lines and the so-called exotic nuclei. They do not occur normally in nature and many of them have never been produced, at least reliably and reproducibly, giving this region the nickname *terra incognita* [4]. Due to the low formation cross-section and short half-lives of exotic nuclei, they are very challenging to produce, observe, and study consistently. One way of accessing them is through the use of fusion-evaporation reactions in which two nuclei are amalgamated into an unstable compound nucleus. This is detailed in Section 2.1. The compound decays into one of several possible daughter nuclei, some of which might be of the exotic variety [5, 6].

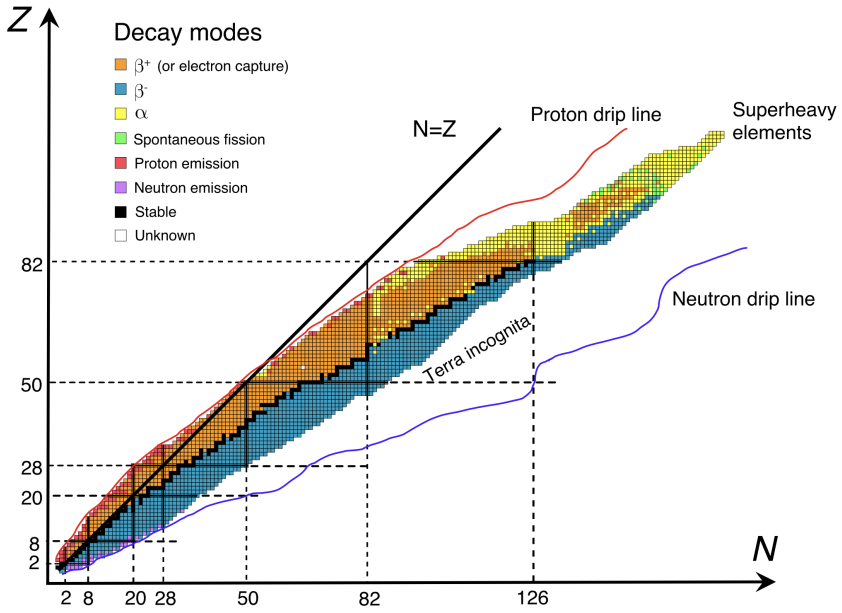

Figure 1: The nuclear landscape showing known nuclei as boxes with the vertical position determined by proton number, Z, and horizontal position determined by neutron number, N. The colours of the boxes represent the decay modes. Black boxes correspond to stable nuclei and the β-stability line. The approximate position of the proton and neutron drip lines (the exact position is still a topic of research) are shown in red and blue, respectively. The dashed lines indicate the so-called magic numbers, which correspond to filled shells and higher stability due to the low degeneracy at the Fermi level. The figure was modified by the author from an original [1] available under a CC BY-SA 3.0 license.

To learn about the energy levels of exotic nuclei, γ rays stemming from the decay of excited states are measured. The main challenge therewith is to separate the γ rays originating from the exotic nucleus from any other γ rays. This is accomplished by implementing a series of detectors that measure the other decay products, including protons, neutrons, and α particles. By requiring coincidences or anti-coincidences between the different detectors, the correct γ rays can be isolated [5]. This Bachelor thesis is focused exclusively on one such detector, namely an array of thallium-activated cesium iodide, CsI(Tl), scintillator detectors. The general operational procedure of scintillator detectors will be delineated in Section 2.2. The pulse shapes obtained from the scintillator detectors may be used to discriminate charged particles such as protons and α particles. The origin of this process, known as pulse-shape discrimination, will be detailed in Section 2.3.

The present thesis is based on experimental data collected at Argonne National Laboratory (ANL) near Chicago, USA, during the summer of 2020. An overview of the experimental setup of this campaign will be presented in Section 3.1. The thesis aims to optimise the pulse-shape discrimination procedure for the Microball detector, which is constituted by a large number of CsI(Tl) detector elements. The Microball detector is presented in greater detail in Section 3.2. The data analysis is performed mainly in the CERN-developed ROOT framework [7]. The computational procedure is outlined in Section 4. The results of the analysis are presented in Section 5. Conclusions and an outlook on possible future developments beyond this work are provided in Section 6.

2 Theory

2.1 Fusion-evaporation reactions

When an accelerated nucleus strikes a stationary target, many different reactions are possible, including elastic and inelastic scattering, direct reactions which involve the rapid transferral of nucleons, fragmentation, fission, or fusion [8]. Fusion-evaporation reactions may occur when the beam energy exceeds the Coulomb barrier between the projectile and target. However, the reaction is most likely for central collisions at comparatively low beam energies of about 3-6 MeV per nucleon. In the reaction, the target and projectile fuse to form a compound nucleus [5, 6]. In the present thesis, data obtained from the bombardment of a ^{24}Mg target with a ^{40}Ca beam, resulting in the reaction

$$^{40}\mathrm{Ca} + {}^{24}\mathrm{Mg} \rightarrow {}^{64}\mathrm{Ge}^{*},$$

are examined. The compound nucleus (here ^{64}Ge) is left in a highly excited state. Usually, the collision will lead to rotation and states with high angular momentum. The nucleus first decays very rapidly (within $\approx 10^{-19}$ s) through the emission (or "evaporation") of light particles, namely α particles, protons, or neutrons. There are often many possible decay pathways, commonly referred to as reaction channels. For instance, the $2p$ channel involves the evaporation of two protons, leading to the ^{62}Zn nucleus. Similarly, the αp channel involves the evaporation of one proton and one α particle, resulting in the nucleus ^{59}Cu [5, 6]. To figure out which channel is active for any given event, it is crucial to be able to distinguish the charged particles accurately. This is the main focus of this thesis and is described further in Section 2.3.

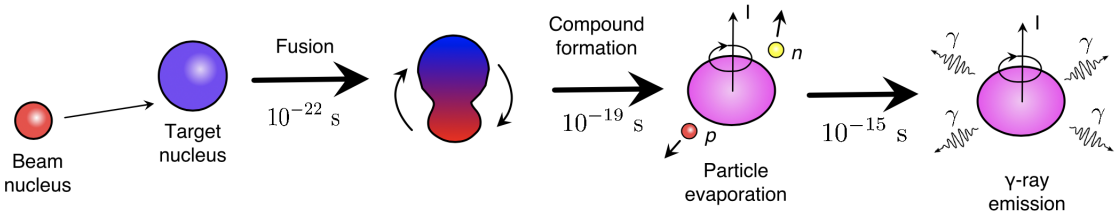

Figure 2: A schematic illustration of the steps of the fusion-evaporation reaction. The timescales indicated are approximate and may depend on the nuclei in question and initial conditions. Figure produced by the author.

Once the residue is no longer excited enough to emit any more particles, it is said to have reached the particle evaporation threshold (see Figure 3). Then, roughly 10^{-15} s after the initial fusion, the nucleus will exclusively emit γ rays. At first, these are statistical, i.e., with a quasi-continuum of energies. However, as the nucleus approaches the yrast line, which is defined as the lowest excitation energy for any given angular momentum, the γ rays become discrete. The discrete γ rays are of major interest for the study of nuclear

structure, as they provide an insight into the spacing of the nuclear energy levels. That is, the γ-ray energy (once corrected for potential Doppler shifts) will correspond to the difference between two nuclear energy levels [5, 6]. The results may be used to compare with theoretical predictions obtained, e.g., using shell-model calculations or Hartree-Fock-Bogoliubov models.

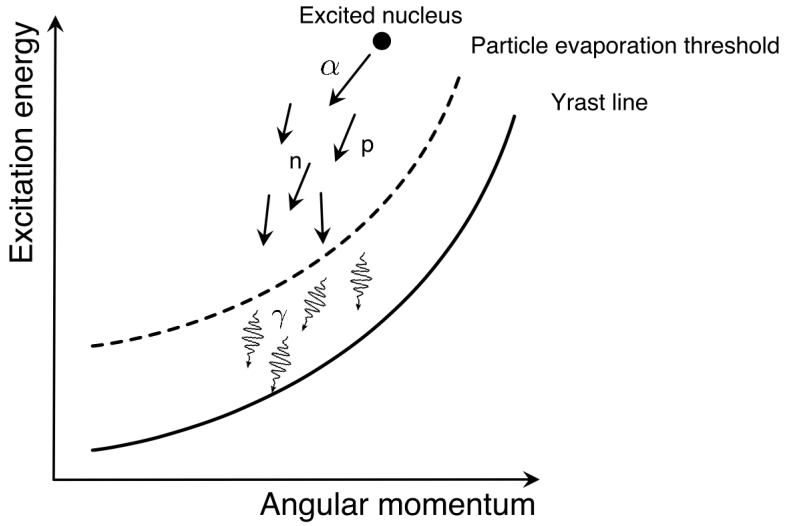

Figure 3: Sketch of the deexcitation of a compound nucleus formed by a fusion-evaporation reaction. The nucleus deexcites primarily through emission of neutrons, protons, and α particles until reaching the particle evaporation threshold (dashed line). It then deexcites through the emission of first statistical, and then, discrete γ rays until reaching the yrast line, generally decreasing its angular momentum in the process. Figure produced by the author.

2.2 Scintillation detectors

The scintillation detector is one of the most common types of particle detectors within nuclear and particle physics. It utilises the fact that some materials emit small flashes of light when struck by a particle or radiation. In inorganic scintillators, the incident particle causes electronic excitations from the valence band to the conduction band. Typically, the scintillator will contain some impurities or dopants which introduce intermediate energy levels. Upon de-excitation over these so-called activator states, lower-energy photons are emitted to which the main scintillation material is translucent. The wavelength of these photons is typically in the visible-to-ultraviolet range. If re-emission occurs within 10^{-8} s, the timescale of atomic transitions, the process is called fluorescence. If the excited state is metastable, there may be a delay between absorption and re-emission, which is referred to as phosphorescence [8, 9, 10]. The time-evolution of the re-emission is often described

in terms of a simple exponential of the form

$$A = \frac{N_0}{\tau} \exp\left(-\frac{t}{\tau}\right), \tag{1}$$

where A is the number of emitted photons per unit time at a time t, N_0 is the total number of emitted photons and τ is the decay time. The rise time, i.e. the time required for the pulse to reach its maximum value, is typically rather short and is here taken to be zero. Some scintillators are not well described by this simple model but may rather have two components, giving a double exponential

$$A = C \exp\left(-\frac{t}{\tau_f}\right) + D \exp\left(-\frac{t}{\tau_s}\right), \tag{2}$$

where τ_f and τ_s denote the decay times of the so-called fast (prompt) and slow (delayed) components whilst C and D are constants. The relative magnitudes of these components can be different depending on the material and what particle is detected [8, 9, 10]. This fact will, as we shall see in Section 2.3, form the basis of pulse-shape discrimination. The fast component is typically dominant although, in particular for inorganic scintillators, the slow component might be significant [9].

The light must then be converted into an electrical signal for further analysis. The photomultiplier tube (PMT) is the most common device utilised for this purpose. However, photodiodes have become increasingly common as a substitute. In the Microball detector, silicon photodiodes are implemented. Such a diode contains a thin p-doped layer and an n-doped layer. Excess electrons from the n-doped side diffuse towards the p-type material while holes from the p-type do the opposite. These recombine and form a layer with few free charge carriers known as a depletion layer. As both the p-side and the n-side are initially electrically neutral, an electric field opposing the diffusion is formed. However, the depletion region can be widened through the application of an external bias. When scintillation photons, which typically have energies of 3-4 eV, hit the depletion region, electrons are excited from the valence band to the conduction band. This requires traversing a band gap which is about 1.1 eV in silicon. The formed electron-hole pairs are separated by the bias and can thus be processed by an attached preamplifier to produce the output pulse [10]. A sketch of a standard photodiode is shown in Figure 4.

Photodiodes have the advantage of being comparatively small, which makes them much more suitable to be placed inside a γ-ray spectrometer. In addition, the quantum efficiency tends to be high as the charge carriers do not need to escape from a surface, as is the case for the photocathode in conventional photomultiplier tubes. Unfortunately, the signal amplitudes obtained from photodiodes are very small compared to those in PMTs, making the signal more sensitive to electronic noise [10].

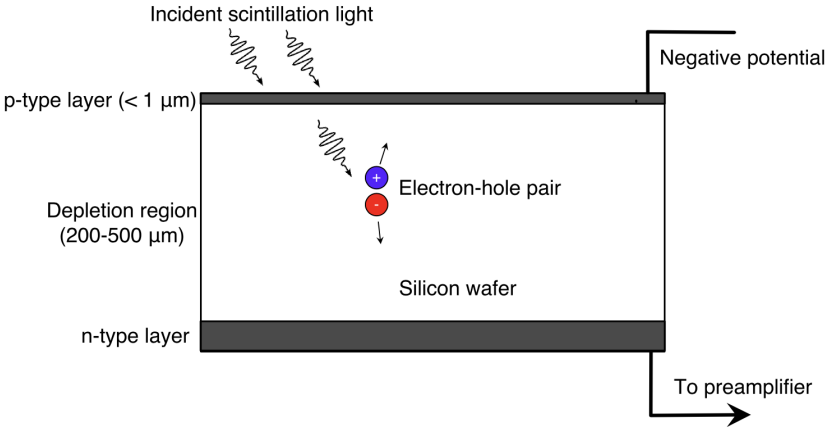

Figure 4: Schematic of a simple silicon photodiode. Further details are in the text. Produced by the author with inspiration from Figure 9.14 in Ref. [10].

Above a minimum threshold energy, the light output of the scintillator increases nearly linearly with the deposited energy. The photodiode is also linear and, therefore, the final signal amplitude will be proportional to the energy. Consequently, the scintillator may be used as an energy spectrometer, although there exist better options for this purpose (e.g. semiconductor detectors). Scintillators with PMTs are, however, often desired for their fast response and recovery times. Minimising the dead time of the detector will enable it to manage higher count rates [8, 9, 10].

2.3 Pulse-shape discrimination

Certain scintillator types allow for the discrimination of different particles through analysis of the shape of the detected pulses. We may recall from Eq. (2) that scintillators exhibit both fast and slow decay components. Both of these components are to some extent dependent on average energy deposited per unit distance $\langle \mathrm{d}E/\mathrm{d}x \rangle$. This quantity is approximately given by the Bethe-Bloch formula which is derived through a quantum mechanical collision model. It states that the average energy loss from a charged particle in a medium is

$$\left\langle \frac{\mathrm{d}E}{\mathrm{d}x} \right\rangle = \left(\frac{e^2}{4\pi\epsilon_0} \right)^2 \frac{4\pi z^2}{m_e c^2 \beta^2} \frac{Z N_A \rho}{A} \left[\ln\left(\frac{2 m_e c^2 \beta^2}{I(1-\beta^2)} \right) - \beta^2 \right], \tag{3}$$

where z denotes the atomic number of the charged particle, Z is the (average) atomic number of the medium, ρ is the density of the medium, A is the (average) molar mass of the medium, I is the average excitation energy of electrons in the medium, β is the relativistic velocity of the charged particle, m_e is the electron mass and N_A is the Avogadro constant [8, 10]. Since protons and α particles have different charges, their energy deposits in the scintillator will be different at the same velocity. Consequently, the ratio between the fast and slow components, and thereby the overall decay time, will be dependent on

which charged particle enters the scintillator [9, 10]. An example illustrating the difference between proton and α-particle pulses is shown in Figure 5.

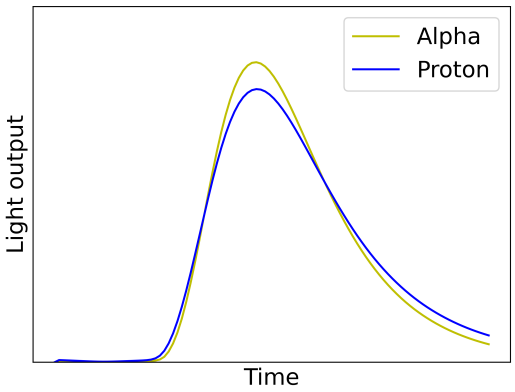

Figure 5: Proton and α-particle pulses observed in a CsI(Tl) scintillator detector. Notice how the α-particle pulse decays more rapidly than the proton pulse. The plot is made using experimental data from one of the detector elements in Microball (cf. Sections 3.2 and 4.1). The pulses have been normalised to have the same total area. Figure produced by the author.

The fundamental reason behind the dependence of the pulse shape on the detected particle is that the fast and slow components stem from deexcitation of different states in the scintillator material. Depending on the energy loss, the states have different probabilities of occupation, which leads to a change in the relative intensities of the components. For alkali halides such as CsI, higher ionisation losses lead to many loosely bound electron-hole quasiparticles called excitons. These excitons propagate through the crystal until reaching an impurity centre. Once arrived, they may be absorbed collectively which excites the impurity into radiative states. This is what gives rise to the fast component. On the other hand, singly free electrons and holes which do not form excitons are captured continuously at the impurities and lead to excitations into metastable states which are inaccessible to the excitons. At lower ionisation densities, as provided by the Bethe-Bloch formula, the formation of excitons is far less probable. This reduces the fast component significantly, thus affecting the pulse shape [9, 10].

One should also note that variations in decay time may be caused by external factors, including temperature and the impurity content of the individual scintillator crystal. Consequently, each individual counter may require its own optimisation procedure to allow for the best possible discrimination [9, 10].

3 Experimental background

This section will seek to briefly describe the experimental setup from which the data in question was obtained. In Section 3.1, a high-level overview of the experimental setup will be provided for context. In Section 3.2, we consider the Microball detector, which this thesis is primarily concerned with. The reader is encouraged to consult, for instance, the MSc thesis by Dalia Farghaly [11] and the PhD theses by Lise-Lotte Andersson [5] and Emma Johansson [6] for a more in-depth discussion of other detector types.

3.1 Overview

The experiment under consideration was performed at Argonne National Laboratory in 2020 with a $^{40}Ca^{19+}$ ion beam at an energy of 106 MeV. The target consisted of a 0.4 mg/cm^2 highly enriched ^{24}Mg foil. The emitted particles are observed in several different detectors, pictured schematically in Figure 6. Firstly, the Gammasphere is a γ-ray spectrometer consisting of up to 110 Compton-suppressed high-purity germanium detectors [12]. The purpose of the spectrometer is to observe the energies of the emitted γ rays and thereby reproduce the energy levels of the daughter nuclei from, for instance, fusion-evaporation reactions (see Section 2.1). In this particular experiment, only 69 detector elements were active. Instead, 30 of the 110 positions were occupied by liquid scintillators for neutron detection. These are intended to allow the selection of one- and two-neutron evaporation channels.

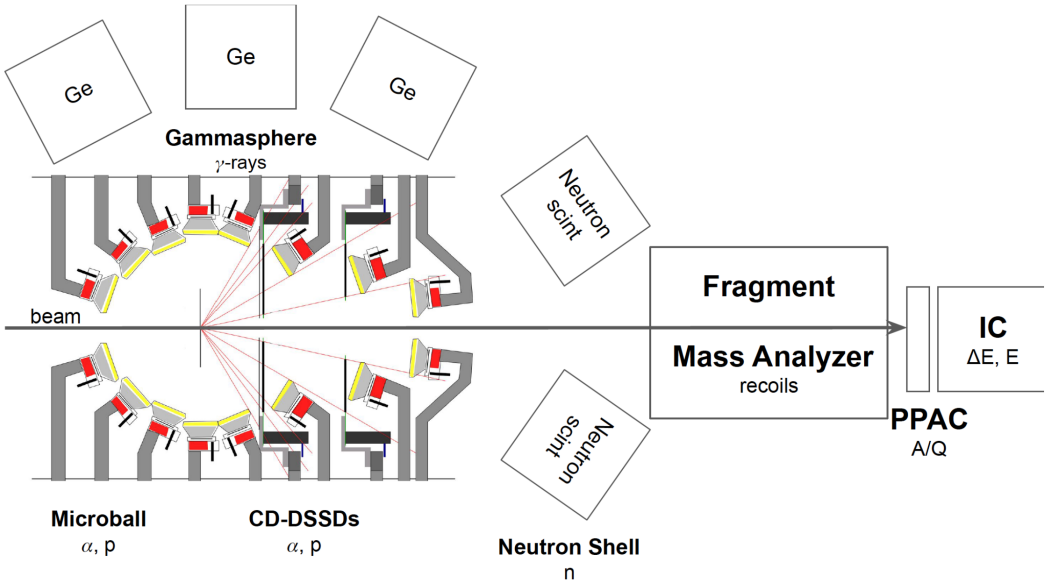

Figure 6: Overview of the experimental setup employed at the experiment at ANL in 2020. The beam hits a target surrounded by the Gammasphere, Microball, DSSDs, and neutron scintillators. The recoiling nuclei are analyzed by the FMA, PPAC, and IC. Further details are in the text. The figure was produced by Yuliia Hrabar and is used with permission.

To detect charged particles, namely protons and α particles, the Microball detector is used as an ancillary detector to the Gammasphere. This thesis is only concerned with the analysis of the data from Microball. It will therefore be described in greater detail in Section 3.2. Placed behind the target chamber and along the beamline is a setup consisting of the fragment mass analyser (FMA), a parallel-plate avalanche counter (PPAC), and an ionisation chamber (IC). The FMA is a mass spectrometer utilised to measure the momentum-to-charge ratio, which helps to reject the primary beam. This is followed by a second separation in terms of mass-to-charge ratio. The PPAC then measures the precise position of the recoils, whereas the IC measures their energy loss, allowing the determination of their proton number. Combining all information allows us to find the species of the recoil nuclei event-by-event.

The ultimate goal of the experimental campaign has been to study nuclei close to the proton drip line such as ^{61}Ga and ^{62}Ge. Since the reaction channels for such nuclei have a relatively low cross-section, it is crucial to effectively distinguish different reaction channels. To accomplish this, one requires coincidences or anti-coincidences between the γ rays in the Gammasphere with the FMA setup, Microball, and/or neutron detectors. In this way, one can efficaciously select the events corresponding to the desired reaction channel.

3.2 Microball detector

The Microball detector was developed by scientists at Washington University in St. Louis. In its standard configuration, it consists of 95 densely packed CsI(Tl) detectors, forming a nearly 4π setup [13]. As mentioned previously, the primary purpose of the detector is to detect charged particles such as protons and α particles, aiding in the selection of charge-specific reaction channels. In addition, the momenta of the particles are used to perform Doppler corrections which improves the energy resolution of the Gammasphere by up to three times [13].

In this experiment, one ring of CsI detectors had been removed and replaced by two circular CD-type double-sided silicon strip detectors (DSSDs). An illustration of the Microball setup including the DSSDs is shown in Figure 7. The DSSDs offer improved granularity as each contains 32 rings and 64 sectors, providing 2048 pixels in all. This allows for better tracking capabilities and the possibility to separate interaction points. Practically all α particles, considering their high mass and them being doubly charged, will be stopped at the latest in the second DSSD. The particles reaching the scintillators behind the DSSDs (rings R2 and R3 in Figure 7) will, in practice, exclusively be lower-energy protons.

The placement of the detectors also has a profound impact on the possibilities for pulse-shape discrimination. Particles that are emitted at backward angles tend to be less energetic than those emitted in the forward direction. This entails that some protons, and an even larger fraction of α particles, will be stopped in the absorber layer of the detectors, yielding no signal. In addition, the difference in decay time between protons and

α particles will be reduced, making it significantly more difficult to separate the two kinds of particles [5]. For this reason, the initial stage of investigation in the thesis was to use the downstream detector elements to study the characteristics of the proton and α-particle pulses, where the separation is relatively straightforward. The insight from this analysis could then be used to improve the separation in upstream detector elements as well.

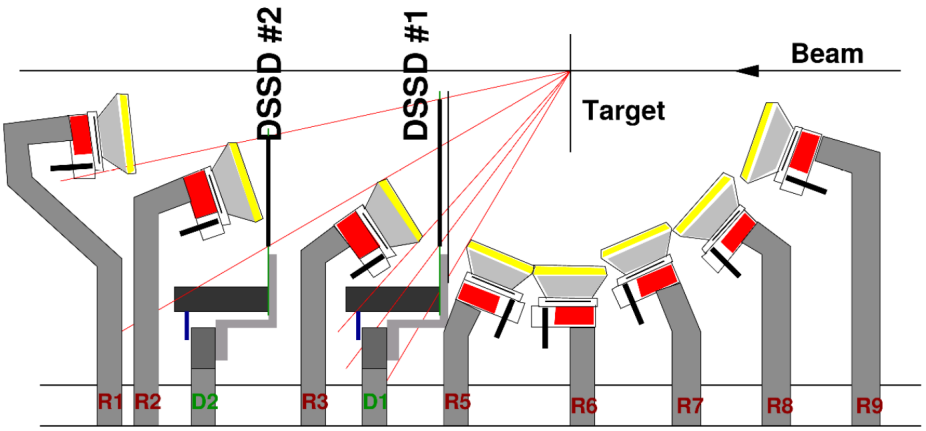

Figure 7: The figure shows a close-up schematic of the cross-section of Microball with its CsI(Tl) scintillator detector elements. Notice how one ring (R4) has been removed. Instead, two rings of DSSDs (D1 and D2) have been inserted. Further details are in the text. The figure was produced by Dirk Rudolph and is used with permission.

4 Method

4.1 Data acquisition, sorting, and merging

Over the course of the experiment, data was collected in runs of around 1 hour each. This is partly as a safety measure in case the data becomes corrupted but it also serves to facilitate data analysis since only a subset of the data needs to be considered at any given time. Overall, 161 runs were recorded corresponding to about 7 TB of raw hexadecimal data files. Three different data acquisition systems (DAQs) were used, called DGS (Digital Gammasphere), DFMA (Digital Fragment Mass Analyser) and WUDAQ (Washington University DAQ). The data analysis is performed through code sections called `GEBMerge` and `GEBSort` which were first developed by ANL [14]. The code is written using ROOT, a computational framework developed by CERN which is implemented primarily in C++ [7].

As three different DAQs are used, the data from each DAQ are first merged by `GEBMerge` for every run. At that point, the data is ordered by timestamp. Next, `GEBSort` sorts the data into events by considering whether the timestamps fall within an event window of

8 µs. They are then further grouped into subevents depending on what detector the data comes from. Each subevent is processed by different parts of the code and information such as timestamp, detector ID, trace, and total energy of each hit are registered. This data is then used to create histograms in a `.root` format for further analysis. In this thesis, it is only the part of `GEBSort` concerned with data from the Microball detector, which is handled by DFMA, that has been considered and modified. The execution of the code and data visualisation was performed on Aurora, a computer cluster provided by LUNARC, the centre for scientific and technical computing at Lund University [15].

The traces from each Microball event are stored in `GEBSort` as arrays with 100 bins. Each bin corresponds to 160 ns. For all digitised pulses, the baseline must be removed, which is accomplished by subtracting the average of, roughly, the first 20 bins.

4.2 Charge-comparison method

The charge-comparison method distinguishes different particle pulses by integrating the pulse along two different intervals. Since the fast component dominates at earlier times and the slow component at later times, the ratio between the two integrals is indicative of the particle type. An illustration is shown in Figure 8. As mentioned previously, the precise pulse shapes depend both on the particular detector as well as how the signal is processed, i.e., which data acquisition system is used. The optimal placement of the integration limits is therefore not known beforehand [16]. Prior to this thesis work, the charge-comparison method was implemented using the same unoptimised integration limits for all detector elements. With the new implementation presented here, a specific set of integration limits can be applied to every detector element.

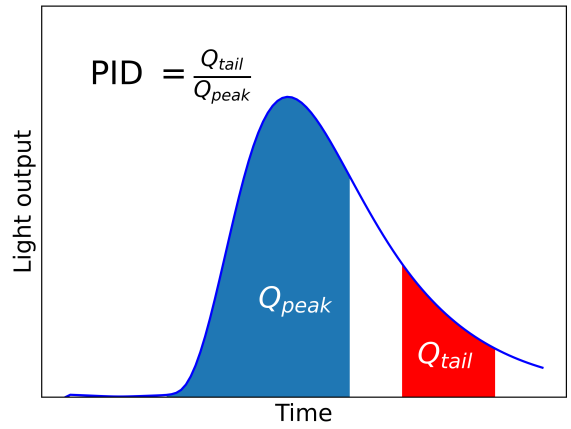

Figure 8: Illustration of the charge-comparison method where two different intervals of the pulse are integrated and the particle identification (PID) ratio is computed. Figure created by the author using pulses obtained from one of the Microball detector elements.

The particle identification (PID) ratios obtained are commonly visualised in 2D histograms. The two types considered within this thesis will henceforth be referred to as `tratio` and `eratio` histograms. In `tratio` diagrams, the PID ratio is plotted against the difference between the timestamp of the event and the leading edge discriminator timestamp. What this corresponds to physically is the time required for the pulse to surpass a certain threshold. As such, it provides a simple estimate of the time of flight of the particle being detected. Since α particles travel slower for any given energy due to their higher mass, this can aid the discrimination further. In `eratio` diagrams, the PID ratio is plotted against the energy of the pulse. For the energy, one can either use the Q_{peak} as shown in Figure 8, or the integral of the whole pulse. Examples of `tratio` and `eratio` histograms, where a clear separation between protons and α particles has been achieved, are shown in Figures 9 and 10, respectively.

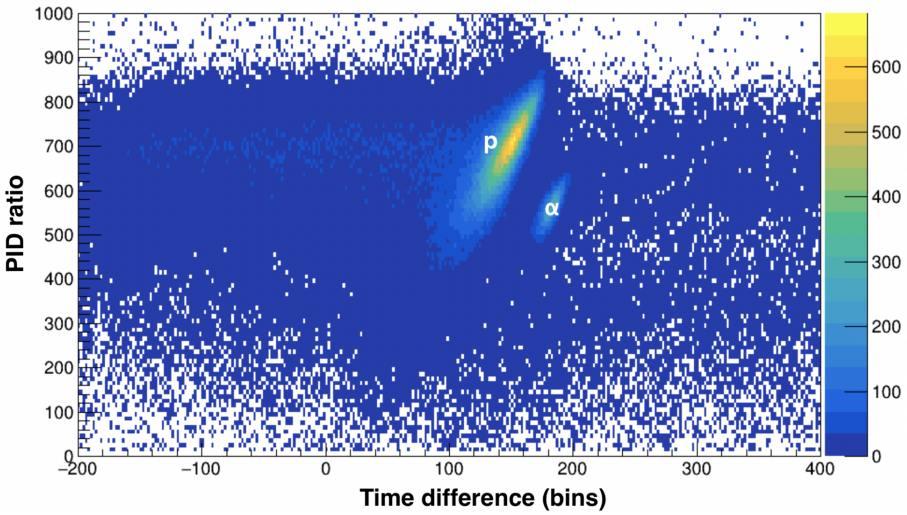

Figure 9: Histogram of `tratio` type for one of the downstream detector elements where a clear separation between protons (labelled p) and α particles (labelled α) is achieved. The colours represent the number of events in each bin. Note that the PID ratio has been rescaled by a factor of 1000. Further details are in the text.

4.3 Cosine similarity measure

Various pattern recognition methods can be used for pulse-shape discrimination, wherein the whole pulse is analysed and compared to reference pulses for different particle types. Similarity measures are used to quantify the similarity of two or more datasets. Owing to its comparatively simple implementation, the cosine similarity measure is a common choice. If we consider two datasets as represented by vectors x and y, the cosine similarity measure is defined as the cosine of the angle θ subtended by the vectors [16]. Just like in

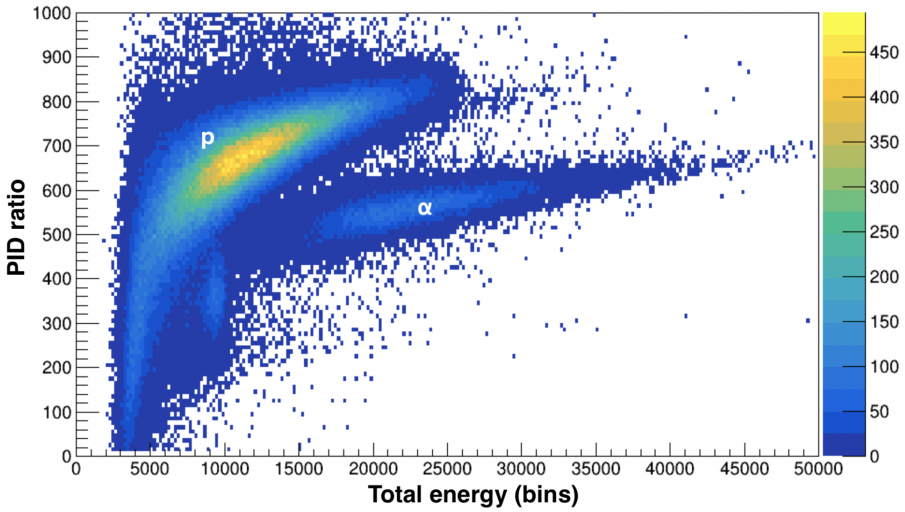

Figure 10: Histogram of `eratio` type for one of the downstream detector elements where a clear separation between protons (labelled p) and α particles (labelled α) is achieved. The colours represent the number of events in each bin. Note that the PID ratio has been rescaled by a factor of 1000. Further details are in the text.

ordinary vector calculus, it is given by

$$\cos\theta = \frac{x \bullet y}{|x||y|}, \tag{4}$$

where $\bullet$ denotes the scalar product and $|x|$ denotes the norm of the vector x. If the vectors have p components each, then explicitly

$$\cos\theta = \frac{\sum_{i=1}^{p} x_i y_i}{\sqrt{\sum_{i=1}^{p} x_i^2}\sqrt{\sum_{i=1}^{p} y_i^2}}. \tag{5}$$

If the vectors x and y are similar, then the angle between them approaches zero and the similarity measure approaches unity. Very dissimilar datasets, i.e. when the vectors are orthogonal, have a cosine similarity measure of zero [16]. The benefit of this method is that, under certain circumstances, the analysis can be performed event-by-event to see immediately which events are likely protons, which are likely α particles, and which are more difficult to ascertain. The challenge is instead to find a good reference vector. Since the pulse shape may vary slightly between different detector elements, one should ideally use detector-specific reference pulses. For instance, one can use averaged pulses from events known to be either protons or α particles.

An alternative and simpler approach is, rather than using a particle pulse template, to instead simply use a step pulse as a reference. Since all elements of the vector y then are

equal to 1, Eq. (6) simplifies to

$$\cos\theta = \frac{\sum_{i=1}^{p} x_i}{\sqrt{\sum_{i=1}^{p} x_i^2}\sqrt{p}}. \tag{6}$$

In this case, it is typical to start the comparison once the pulse has passed a certain threshold value, e.g. 10 percent of its total amplitude. The length of the time interval compared (p) can be either fixed or variable (pulse-dependent). The numerator of the relation is now simply the integral of the pulse, as would be used in the charge-comparison method. In the denominator, we find the signal power, which is another parameter used for PSD (and forms the basis of a method called *signal power analysis*). Finally, the $\sqrt{p}$ factor can, if a variable time window is used, reflect the rise time of the pulse, yet another PSD parameter (used in the technique called *rise time discrimination*). Consequently, the cosine similarity measure with a step reference pulse will, despite its simple appearance, contain much information about the pulse characteristics [17].

4.4 Performance measurement

While there are many ways of performing pulse-shape discrimination, one wishes to choose the method that, while being reasonably simple to implement, yields the best possible discrimination between particle types. While the evaluation can to some extent be done by eye, it is desirable to quantify the performance of the specific algorithm. One such quantisation can be achieved by considering the data along a straight line connecting the central peaks of the different particle types as illustrated in Figure 11(a).

Typically, particularly for the `tratio` histograms, such lines will be slanted. Since the data is partitioned into rectangular bins, it is not straightforward to integrate along a slanted line. Consequently, the data should first be rotated so that the peaks lie along a horizontal line. If we consider data points of the form (x, y) which we wish to rotate around the point (a, b), this can be accomplished by first subtracting the coordinates (a, b) so that we receive the coordinates relative to the rotation point. This is followed by multiplication of an ordinary rotation matrix for counterclockwise rotation about the origin by an angle θ. After adding back (a, b) we receive the rotated coordinates (x', y') which can be plotted in a histogram as usual. In formulas, the relation becomes

$$\begin{bmatrix} x' \\ y' \end{bmatrix} = \begin{bmatrix} \cos\theta & -\sin\theta \\ \sin\theta & \cos\theta \end{bmatrix} \begin{bmatrix} x-a \\ y-b \end{bmatrix} + \begin{bmatrix} a \\ b \end{bmatrix}. \tag{7}$$

With the rotated histogram, we can simply perform a horizontal projection, i.e. looking at the bin contents along a horizontal line. An example of a plot obtained using this method is illustrated in Figure 11(b). To evaluate how good the separation between the two peaks is, a dimensionless figure of merit (FOM) was computed by taking the distance between the peaks, d, and dividing by the sum of the full width at half maximum (FWHM) of each

peak [16], i.e.

$$\mathrm{FOM} = \frac{d}{\mathrm{FWHM}_p + \mathrm{FWHM}_\alpha}. \tag{8}$$

Note that this FOM will not change upon rotation or linear rescaling of the axes (since both d and the FWHM are scaled by the same factor) as long as the binning is sufficiently fine. The FWHM and peak distances can be determined by fitting Gaussian functions to each of the peaks. The distance d is then obtained as the difference between the peak centroids whereas the FWHM is related to the standard deviation σ of the Gaussian as

$$\mathrm{FWHM} = 2\sqrt{2\ln 2}\,\sigma \approx 2.355\sigma. \tag{9}$$

The uncertainties from the fit of the parameters can also be propagated to provide an uncertainty for the FOM.

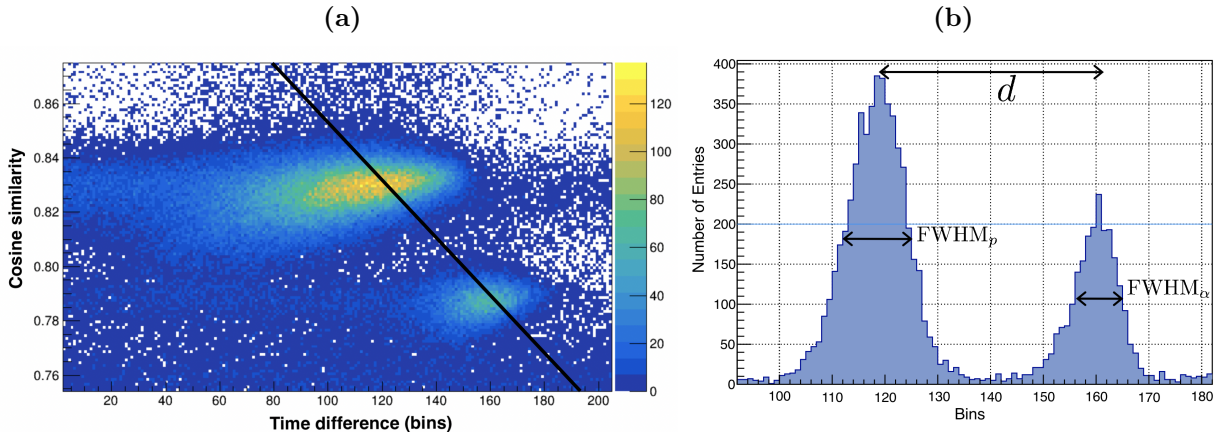

Figure 11: The process used to compute the FOM is demonstrated. **Panel (a)**: A straight line (shown in black) connecting the two centres of the peaks corresponding to each particle type is chosen and the data is rotated so that the line becomes horizontal. A horizontal projection then gives a one-dimensional histogram. **Panel (b)**: The distance between the peaks, d, and the FWHM of each peak are determined to compute the FOM in accordance with Eq. (8).

5 Results and analysis

5.1 Averaged proton and α-particle pulses for downstream detector elements

To gain some first insight into how the proton and α-particle pulses look, averaged pulses were created for each particle type. Using the charge-comparison method, a substantial number of `tratio` and `eratio` histograms were created utilising various values for the integration limits. Upon visual inspection of the histograms, a suitable set of parameters was chosen for each of the detector elements. Initially, this was done only for the downstream detector elements since the separation is comparatively good for a wide range of parameter values. See Figures 9 and 10 for the histograms obtained for one of the detector elements.

Two-dimensional gates were created in the `tratio` diagrams to select known protons and α particles. At this point, the gates were drawn rather conservatively to avoid mixing the different particle types. Separate averaged traces were created for protons and α particles by only adding the traces corresponding to events within the respective two-dimensional gates. The traces were extracted from ROOT into a `.txt` file by writing a ROOT-compatible C-script. The file was then read into a Jupyter Notebook for more convenient analysis. To illustrate the difference between the proton and α-particle pulses, both were normalised to the same amplitude. Exponential functions were fitted to the tails of the pulses, defined here to start 15 bins (2.4 µs) after the peak. An example of such a fit is shown in Figure 12.

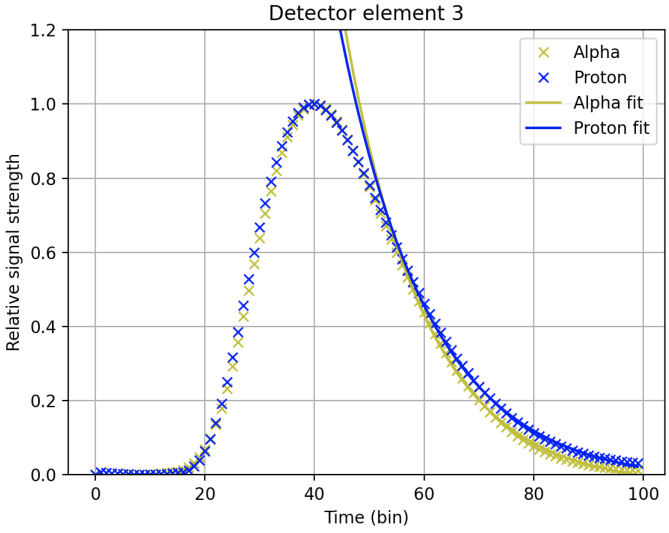

Figure 12: Averaged pulses from α particles and protons in one detector element are shown as yellow and blue crosses respectively. Note that the pulses have been normalised to the same amplitude. Exponential fits were made to both datasets, shown as solid lines, starting 15 bins after the peak.

The decay times obtained by this method are listed in Table 1. For all of the detector elements, the α-particle decay time is shorter than the proton decay time, although the absolute difference varies within a range of 250-500 ns. This observation is in qualitative agreement with the theoretical argument laid out in Section 2.3. However, we can also note that there is significant variation in the overall decay times between detector elements. For example, the proton decay times in detector elements 3-4 are shorter than the decay times for α particles in detector elements 1-2. Consequently, one cannot simply look at the decay time to determine the particle type without considering the characteristics of the particular detector element.

Table 1: Measured decay times of protons and α particles in the downstream detector elements. The values are obtained by fitting exponential functions to the tails of the pulses.

Detector ID	Decay time (µs)	
	α particles	Protons
1	2.97(3)	3.45(4)
2	2.99(4)	3.39(5)
3	2.41(5)	2.67(4)
4	2.34(5)	2.70(4)
5	2.68(4)	2.97(4)
6	2.69(3)	3.04(4)

While the simple approach described above produced satisfactory results for the downstream detector elements, it did not prove equally useful for the upstream detector elements. Despite varying the integration limits over a wide range of values, only a modest improvement, if any, could be noticed compared to the earlier implementation. Moreover, manually adjusting the integration limits is a time-consuming procedure which is difficult to automate considering the large data structures and many optimisation parameters, namely all four integration limits, not to forget the proper range of the background subtraction. Consequently, it was motivated to explore alternative approaches including the cosine similarity measure.

5.2 Evaluating the cosine similarity measure

As explained in Section 4.3, using a step pulse which rises from 0 to 1 as the pulse crosses 10 % of its amplitude is one possible reference pulse. This approach will be evaluated in the following section. To that end, `eratio` histograms were created but where the cosine similarity measure is plotted on the vertical axis rather than the PID ratio. An example of this is shown in Figure 13. As we can see, the protons and α particles form a nearly horizontal line at higher energies. This means that all particles of the same type have approximately the same similarity measure. This fact simplifies the computation of the FOM, as a simple vertical projection can be used. The colour-inverted region of Figure 13 shows 10 adjacent bins for which a projection can be performed. The reason one wishes, if

possible, to include more bins is to achieve higher statistics, which is particularly relevant for the comparatively small number of α particles. Looking back at Figure 10, we see that this horizontality is not necessarily obtained for the charge-comparison method. Such histograms were rotated if necessary as described in Section 4.4. The reason there is a wide range of similarities at lower energies (left of the dashed line in Figure 13) is likely the presence of spurious pulses and noise events which have disparate shapes.

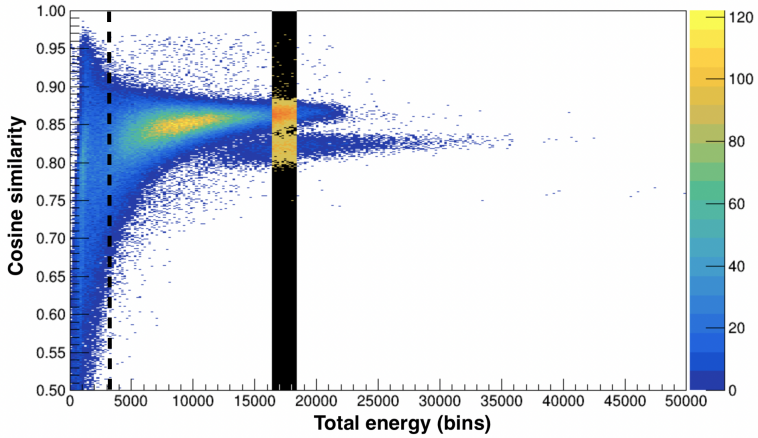

Figure 13: Histogram showing the cosine similarity with respect to a step reference pulse against the full energy of the event for one of the detector elements. The colour-inverted region illustrates where a projection can be performed to compute the FOM. Further details are in the text.

The performance of the charge-comparison method and cosine similarity measure was compared for all six detector elements in ring 1 (see Figure 7) using the FOM described in Section 4.4. To reflect the difference between different choices of integration limits, two sets of parameter values were utilised for the charge-comparison method. The first has a narrower set of gates (i.e., smaller integration regions similar to those used in the former analogue signal treatment) whereas the second uses a wider set. To facilitate a fair comparison, the same number of bins were used for the projection and the same energy range was used for all three PSD methods, although the energy range may vary slightly from detector to detector. In general, the performance was measured for the energy range where the discrimination tended to be worst, typically at lower energies. This is motivated by the fact that it is most relevant to have a good separation at these energies. The results are summarised in Table 2.

Table 2: The FOM values obtained from `eratio` histograms using the charge-comparison method and cosine similarity measure respectively for the six downstream detector elements in ring 1.

Det. ID	Charge-comparison (narrow)	Charge-comparison (wide)	Cosine similarity
1	1.27(6)	1.19(4)	1.36(7)
2	1.00(4)	0.91(8)	1.08(7)
3	1.37(3)	1.62(4)	1.53(3)
4	1.28(2)	1.35(3)	1.37(3)
5	1.24(2)	1.39(2)	1.35(2)
6	1.29(3)	1.43(5)	1.39(11)

We can see that using the wider integration limits leads to better performance for all but the first two detector elements. The cosine similarity is on-par with the wide-gate charge-comparison method, with slightly better performance in detector elements 1 and 2 and slightly worse in detector element 3. However, the relatively large uncertainties make it difficult to conclusively say one method is better than another.

One further point to keep in mind when evaluating this comparison is that, as mentioned previously, in the `eratio` histograms the particle regions may not necessarily correspond precisely to horizontal lines but may rather be curved, as Figure 10 illustrates. This means that the discrimination could be better at some energies and worse at others, a fact not properly reflected by the FOM, but which can be visually noted when inspecting the histograms. However, the comparison certainly demonstrates that the cosine similarity measure is a legitimate alternative to the traditional charge-comparison method which may improve the discrimination for certain detectors and energy ranges. Furthermore, the fact that the particle regions are almost horizontal at higher energies may be considered a desirable trait. In particular, the value of the similarity obtained proved to be nearly the same for all detector elements (with the cross-over point at a little over 0.80), something which cannot be said for the PID ratio. This means that one can directly (with some precaution) determine the type of particle without the need to resort to visual inspection of histograms.

A similar investigation of the three types of PSD was undertaken for the `tratio` histograms. This time, the precise procedure described in Section 4.4 was followed, including prior rotation. It should be noted that this metric will be slightly different than for the `eratio` since, in this case, the FOM is evaluated along a line connecting the central peaks. Thus, the evaluation is not exclusively for the lower energies (where the discrimination is worst). The results are summarised in Table 3.

Table 3: The FOM values obtained from `tratio` histograms using the charge-comparison method and cosine similarity measure respectively for the six downstream detector elements in ring 1.

Det. ID	Charge-comparison (narrow)	Charge-comparison (wide)	Cosine similarity
1	1.24(4)	1.16(4)	1.19(5)
2	0.89(9)	0.85(4)	1.01(8)
3	1.59(5)	1.42(5)	1.87(9)
4	1.67(6)	1.54(5)	1.87(3)
5	1.38(4)	1.40(3)	1.73(4)
6	1.61(5)	1.89(4)	2.01(7)

Here, we can note that the cosine similarity measure outperforms the charge-comparison method for all but the first detector element. The reason we see better performance is most likely the aforementioned fact that there is comparatively little spread in the similarity measure for different energies. This means that the particle regions become more compact. When projected along a line, we will thus measure a smaller FWHM and a higher FOM.

It should be kept in mind that once a FOM of above 1.5 is achieved, the peaks are quite well separated and so, for the final implementation, it is not particularly significant which method is used. However, since we see significantly increased performance for two of the three detectors that before had the worst separation, namely detectors 2 and 5, it seems wise to use histograms with the cosine similarity measure, at the very least as a complement. Hopefully, this will lead to an overall refinement in the final γ-ray spectra, which are the final products this experimental campaign seeks to produce.

Another interesting feature of the cosine similarity measure is that it can more easily distinguish random background events. Consider the example shown in Figure 14, where one of the `tratio` diagrams is made using the charge-comparison method and the other using the cosine similarity measure. As can be seen, there is a horizontal band of events which, in panel (a), lies around the region between the proton and α-particle peaks. In panel (b), obtained with the cosine similarity measure, this band is shifted towards a lower similarity of about 0.75. This is desirable since it entails an improved signal-to-noise ratio. It should be noted that it is possible to shift these events to some extent also using the charge-comparison method, by utilising a different set of integration limits. The benefit of the cosine similarity measure is that this separation comes without any manual tweaking of parameters, which could potentially worsen the discrimination. While this effect is partially reflected by the FOM (since it will lead to a slightly larger FWHM), the improved signal-to-noise ratio should be considered in and of itself when evaluating the performance of different approaches.

(a) Charge-comparison method **(b)** Cosine similarity measure

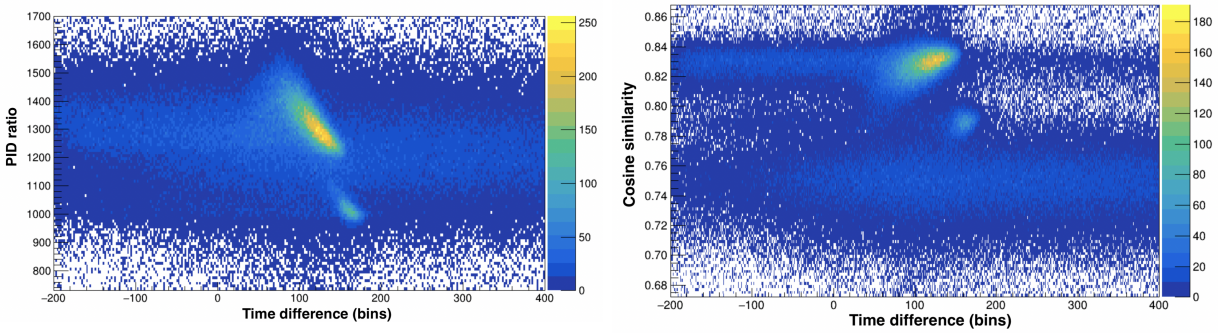

Figure 14: A comparison of two histograms of `tratio` type obtained using the charge-comparison method in panel (a) and cosine similarity measure in panel (b). Note the shifting of the band of random background events. Further details are in the text.

5.3 Optimising for further upstream detector elements

For the detector elements in ring 5 and beyond, it was difficult to see any particularly clear separation in the `tratio` histograms using either the PID ratio or cosine similarity measure with respect to a step pulse on the vertical axis. However, an inspection of an `eratio` histogram obtained with the cosine similarity measure, shown in Figure 15, does provide some insight.

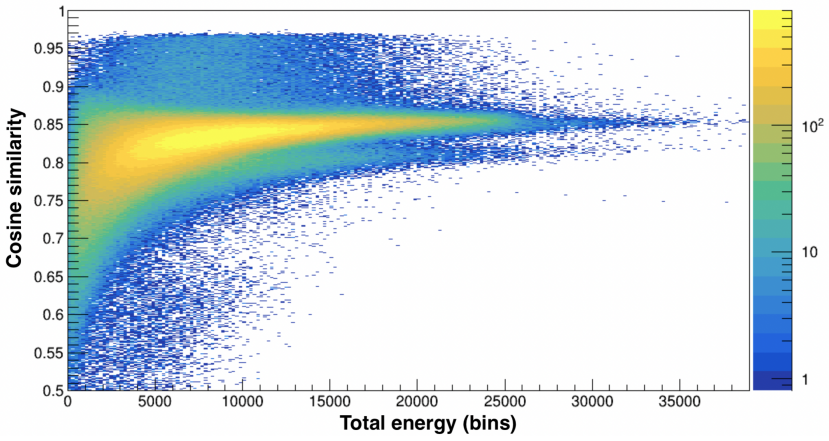

Figure 15: A histogram of `eratio` type showing the cosine similarity using a step function as reference pulse against the total energy for a detector element in ring 5. Note that a logarithmic scale is used in determining the colouring to more clearly visualise the overall small number of α particles.

As we can see, the separation between α particles and protons is in fact fairly noticeable at higher energies. In an attempt to improve discrimination also at lower energies, an

averaged α-particle pulse acquired during the procedure of Section 5.1 was used as reference pulse. The result for one of the detector elements is shown in Figure 16 although similar trends were observed for all detector elements in this ring. A comparison is made with a plot obtained using the previous simple charge-comparison approach. In Figure 16(a), it is difficult to immediately distinguish any α particles, although one can guess that some portion of the events just below the central peak for the protons is constituted by α particles (highlighted with a dashed line). In Figure 16(b), there is a more obvious "appendix" of events (highlighted with a solid line) sticking out at a similarity close to unity. This makes sense as we expect the α-particle pulses to show high similarities, simplifying the identification of the correct region. Although the separation is improved somewhat, it is still significantly worse than in Section 5.2. Due to the shape of the proton and α-particle regions, it is futile to apply the evaluation procedure of Section 4.4.

(a) Charge-comparison method **(b)** Cosine similarity measure

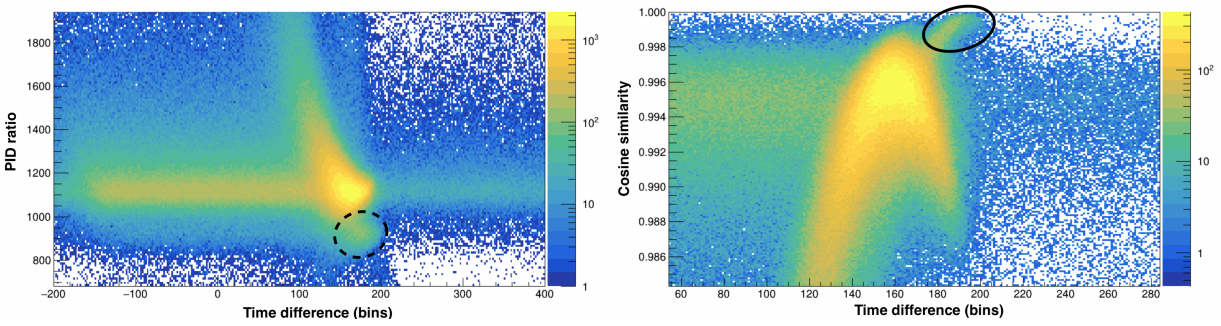

Figure 16: A comparison of two histograms of `tratio` type. In panel (a), the conventional charge-comparison method is employed. In panel (b), an α-particle reference pulse is used to compute the cosine similarity measure, which is then plotted on the vertical axis. Further details are in the text.

As this technique does show some promise in improving the discrimination, a natural extension is to consider detector-specific reference pulses. Such reference pulses are available as, during the experiments, a calibration source of ^{249}Cf with an activity of 3.3 µCi was measured for a few runs. ^{249}Cf and its daughter ^{245}Cm are both comparatively long-lived and decay purely by α decay. Consequently, we expect the pulses obtained to exclusively stem from α particles. The sorted files from the calibration runs were merged and averaged pulses for each detector element were created. These were then used as references in the computation of the cosine similarity measure for the rest of the dataset. Since different triggering schemes were used between calibration and during beam time, the pulses are not initially aligned in time. Consequently, the maxima of both the reference pulses and the averaged pulses during the main experiment were determined. The reference pulse was then shifted in time upon computation of the similarity. Typical results are shown in Figure 17 before and after shifting the reference pulse.

Figure 17 leads to a surprising observation, namely that in many cases the unshifted pulses yield better separation. Notice how for the unshifted pulses, the proton and α-particle regions are spread out in wider bands with limited overlap. Beware of the different scales used in the two panels, as the observed pulses expectedly have a higher similarity with respect to the correctly aligned (shifted) reference pulses. The shifted pulses gave quite compact particle regions, particularly for the α particles which have a similarity very close to unity, as is expected. However, the proton and α particles do now have significant overlap, as illustrated in Figure 17(b). This leads to the conclusion that using a time-aligned reference pulse may not always be the preferred option. Further investigation is necessary to find an optimal strategy, although using the similarity to α-particle reference pulses appears to be a promising approach. In fact, with an appropriate amount of shifting back or forth, the proton and α-particle regions can be almost completely separated for all detector elements in ring 5, as well as for some detector elements even further upstream.

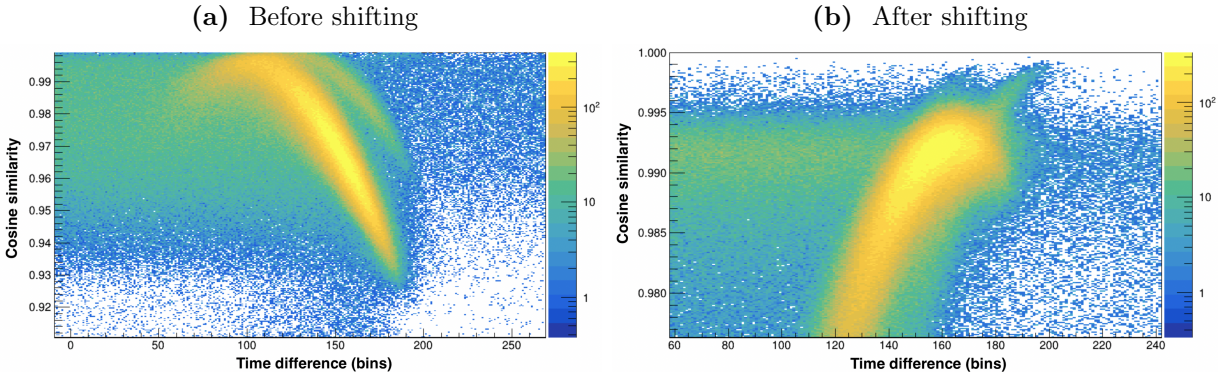

Figure 17: A comparison of two histograms of `tratio` type obtained by computing the cosine similarity with respect to a detector-specific α-particle reference pulse. For panel (a), the original pulse is used. For panel (b), the reference pulse has been shifted in time to have its maximum align with the averaged pulse during the main experiment. Further details are in the text.

6 Conclusions and outlook

Recent advances in the field of digital circuits and the development of fast analog-to-digital converters have enabled the digitisation of pulses from detectors aimed at charged-particle measurements. This provides great flexibility in the development of techniques and algorithms to extract information for PSD. The charge-comparison method is a classical method which has been used in the analogue realm for many decades. With the digitised pulses, there is now a greater possibility to modify the integration limits detector-by-detector *a posteriori*. This fact has been used in this work to improve the discrimination of protons and α particles in the CsI(Tl) detectors in the Microball detector array.

In addition, this work has explored the cosine similarity measure, a simple pattern recognition method which would have been relatively complicated to implement before the advent of digitised pulses. As has been demonstrated, the cosine similarity measure constitutes a viable alternative to the charge-comparison method, both with a simple step pulse as reference or using detector-specific α-particle reference pulses. The cosine similarity measure also possesses certain desirable properties which are not necessarily achieved within the charge-comparison method, including the shifting of background events and the possibility of flagging events without the need for prior visual inspection of histograms. Using the similarity measure has led to a noticeable improvement in certain detector elements, particularly detector elements 2 and 5 and detector elements situated further upstream.

Although this work has provided noticeable improvements in the separation of protons and α particles in ring 5 of the Microball detector, more remains to be investigated. Particularly, it would be interesting to further explore why reference pulses shifted in time seem to produce better separation. Any conclusions drawn could be helpful in the optimisation of even further upstream detector elements. Although there are comparatively few α particles, identifying them would be an important step in facilitating the creation of cleaner yet more telling γ-ray spectra.

The procedures described here will eventually be used for the analysis of the experiment as a whole, undertaken primarily by the co-supervisor of this project within the scope of her doctoral thesis. Most likely, two-dimensional gates will be implemented using histograms of both `tratio` and `eratio` type to produce the final spectra. By using histograms obtained both using the charge-comparison method and cosine similarity measure, a further opportunity to compare the two methods will become available.

This work is by no means an exhaustive survey of the many PSD techniques which have been developed, and which could beneficially be explored and compared with the results presented here. There are other pattern recognition methods besides the cosine similarity measure such as principal component analysis. In this method, reference pulses are used to form a data covariance matrix. By solving an eigenvalue equation, the principal components of any unknown pulse can be calculated and used to discriminate between par-

ticle types. Another avenue to explore is frequency domain methods, in which a Fourier transform of the pulse is performed and various discrimination parameters computed [16].

In the long term, it would be desirable to utilise machine learning algorithms which can autonomously, with limited human input, determine whether a given pulse corresponds to a proton or an α particle. There are two potential challenges with this approach. Firstly, the significant dependence of the signal on the particular detector element and its placement relative to the beamline means that something which looks like a proton in one detector may, at first comparison, look more like an α particle in another. Hence, the algorithm will need to take information about the detector as input. Secondly, to achieve a good machine learning algorithm, a very substantial number of known proton and α-particle pulses are needed to train the algorithm. While it is certainly possible to envision a solution which overcomes these issues, this is certainly beyond the scope of this work. However, recent efforts have been made in this field, particularly for the discrimination of neutrons and γ rays [18, 19], which illustrate the potential of this approach.

References

[1] User Napy1kenobi on Wikimedia Commons. *Table isotopes.svg.* 2008. Available from `https://commons.wikimedia.org/wiki/File:Table_isotopes.svg` (retrieved on 2022-02-05).

[2] S.-G. Nilsson, I. Ragnarsson. *Shapes and shells in nuclear structure.* Cambridge: Cambridge University Press; 1995. pp. 1-26.

[3] J. S. Lilley. *Nuclear Physics: Principles and Applications.* Chichester: Wiley; 2001. pp. 13-17.

[4] P. Chomaz. Introduction: The Terra Incognita of exotic nuclei. *C. R. Physique.* 2003;4(4-5):419-432. `https://doi.org/10.1016/S1631-0705(03)00058-6`.

[5] L.-L. Andersson. *A Trilogy of Mass $A = 61$: Superdeformed Structures, Exotic Decay, and Isospin Symmetry.* Lund: Mediatryck; 2008. pp. 5-36.

[6] E. Johansson. *Nuclear Structure and Exotic Decays; Doubly-Magic ^{56}Ni and Semi-Magic ^{58}Ni.* Lund: Mediatryck; 2009. pp. 19-27.

[7] ROOT Team. *ROOT Data Analysis Framework.* 2021. Available from `https://root.cern` (retrieved on 2022-02-19).

[8] K. S. Krane. *Introductory Nuclear Physics.* 2nd edition. New York: Wiley; 1988. pp. 192-213, 378-440.

[9] W. R. Leo. *Techniques for Nuclear and Particle Physics Experiments: A How-to Approach.* Berlin-Heidelberg: Springer-Verlag; 1987. pp. 149-167.

[10] G. F. Knoll. *Radiation Detection and Measurement.* 3rd edition. New York: Wiley; 2000. pp. 29-43, 219-259, 287-291.

[11] D. Farghaly. *Nuclear Structure near the Proton Drip Line: A Search for Excited States in ^{62}Ge.* 2022. MSc thesis from Lund University.

[12] I.-Y. Lee. The GAMMASPHERE. *Nucl. Phys. A.* 1990;520:c641-c655. `https://doi.org/10.1016/0375-9474(90)91181-P`.

[13] M. Devlin, J. Elson, J. T. Hood, P.-F. Hua, D. R. LaFosse, M. R. Maier, D. G. Sarantites, J. E. Sarantites, L. G. Sobotka. "The Microball": Design, instrumentation and response characteristics of a 4π-multidetector exit channel-selection device for spectroscopic and reaction mechanism studies with Gammasphere. *Nucl. Instrum. Methods Phys. Res. Sect. A.* 1996;381(2-3):418-432. `https://doi.org/10.1016/S0168-9002(96)00785-1`.

[14] Argonne National Laboratory. *Receivers/GEBMerge/GEBsort.* 2020. Available from `https://wiki.anl.gov/gsdaq/Receivers/GEBMerge/GEBsort` (retrieved on 2022-03-02).

[15] LUNARC. *LUNARC - Lund University.* 2022. Available from https://www.lunarc.lu.se (retrieved on 2022-03-02).

[16] M. Nakhostin. *Signal Processing for Radiation Detectors.* Hoboken: Wiley; 2018. pp. 483-498.

[17] M. Nakhostin. A General-Purpose Digital Pulse Shape Discrimination Algorithm. *IEEE Trans. Nucl. Sci.* 2019;66(5):838-845. https://doi.org/10.1109/TNS.2019.2910153.

[18] H. Arahmane, E.-M. Hamzaoui, Y. B. Maissa, R. C. E. Moursli. Neutron-gamma discrimination method based on blind source separation and machine learning. *Nucl. Sci. Tech.* 2021;32:18. https://doi.org/10.1007/s41365-021-00850-w.

[19] E. Doucet, T. Brown, P. Chowdhury, C. J. Lister, C. Morse, P. C. Bender, A. M. Rogers. Machine learning n/γ discrimination in CLYC scintillators. *Nucl. Instrum. Methods Phys. Res. Sect. A.* 2020;954:161201. https://doi.org/10.1016/j.nima.2018.09.036.